Ground deformation and source geometry of the August 24, 2016 Amatrice earthquake (Central Italy) investigated through analytical and numerical modeling of DInSAR measurements and structural-geological data

G. Lavecchia[(1)], R. Castaldo[(2)], R. de Nardis[(1)], V. De Novellis[(2)], F. Ferrarini[(1)], S. Pepe[(2)], F. Brozzetti[(1)], G. Solaro[(2)], D. Cirillo[(1)], M. Bonano[(2)], P. Boncio[(1)], F. Casu[(2)], C. De Luca[(2)], R. Lanari[(2)], M. Manunta[(2)], M. Manzo[(2)], A. Pepe[(2)], I. Zinno[(2)] and P. Tizzani[(2)]

[1] CRUST-DiSPUTer - Università di Chieti-Pescara "G. d'Annunzio", Campus Universitario, Chieti Scalo, Italy

[2] Istituto per il Rilevamento Elettromagnetico dell'Ambiente - Consiglio Nazionale delle Ricerche (IREA-CNR), via Diocleziano 328, 80124, Napoli, Italy.

Corresponding author: Pietro Tizzani (tizzani.p@irea.cnr.it)

Keywords: Amatrice 2016 earthquake; active normal faults; 3D source geometry; DInSAR measurements; analytical modeling; Finite Element modeling

This article has been accepted for publication and undergone full peer review but has not been through the copyediting, typesetting, pagination and proofreading process which may lead to differences between this version and the Version of Record. Please cite this article as doi: 10.1002/2016GL071723

Abstract

We investigate the ground deformation and source geometry of the 2016 Amatrice earthquake (Central Italy) by exploiting ALOS2 and Sentinel-1 co-seismic DInSAR measurements. They reveal two NNW-SSE striking surface deformation lobes, which could be the effect of two distinct faults or the rupture propagation of a single fault. We examine both cases through a single and a double dislocation planar source. Subsequently, we extend our analysis by applying a 3D Finite Elements approach jointly exploiting DInSAR measurements and an independent, structurally-constrained, 3D fault model. This model is based on a double fault system including the two Northern Gorzano and Redentore-Vettoretto faults (NGF and RVF) which merge into a single WSW-dipping fault surface at the hypocentral depth (8 km). The retrieved best-fit co-seismic surface deformation pattern well supports the exploited structural model. The maximum displacements occur at 5–7 km depth, reaching 90 cm on the RVF footwall and 80 cm on the NGF hanging-wall. The von Mises stress field confirms the retrieved seismogenic scenario.

1. Introduction

On 24 August 2016 (01:36 UTC) the intra-Apennine extensional fault system of Central Italy released a M_L 6.0 destructive earthquake [Tinti et al., 2016] between the towns of Norcia and Amatrice (**Figure 1a**). The main shock produced widespread damages and fatalities, devastating several localities and killing about 300 people. The main event was followed by a significant aftershock (M_L 5.4), located 15 km to the NW; the seismic sequence is still ongoing.

After one week, the epicentral area reached a length of about 30 km, in the NNW-SSE direction, largely developing at the hanging-wall of the WSW-dipping active extensional Vettore and Gorzano faults (VF and GF, respectively, see **Figure 1b**). The main event was located at a depth of about 8 km; the fault plane solution was almost purely extensional with NNW-SSE striking focal planes [TDMT in http://cnt.rm.ingv.it/tdmt.html].

After two months, on 26 October (19:18 UTC), another major earthquake (M_L 5.9) occurred 25 km to the NW and few days later, on 30 October (06:44 UTC), a third major earthquake (M_L 6.5) nucleated in between the first two. The overall 2016 Central Italy sequence extends for a length of ~55 km in the NNW-SSE direction, largely developing at the hanging wall of the WSW-dipping active Vettore and northern Gorzano faults.

In this paper, we focus on the ground deformation and source geometry of the 24 August event, referred hereafter to as Amatrice Earthquake (AEQ), which was the only event occurred at the time of this paper submission.

The AEQ epicentral area has been imaged by several space-borne synthetic aperture radar (SAR) sensors which allowed, through the differential interferometric SAR (DInSAR) technique [Franceschetti and Lanari, 1999], retrieval of the co-seismic displacements. In particular, after one week following the main event several DInSAR deformation maps (interferograms) were generated, using images acquired from ascending and descending orbits and from radar sensors operating at different frequencies: Advanced Land Observing Satellite-2 (ALOS2), at L-band; Sentinel-1 (S1), at C-band; COSMO-SkyMed (CSK), at X-band. Note also that the time intervals of the exploited ascending and descending interferograms typically does not allow us to discriminate the surface displacement effects of the main event from those of the major aftershocks. However, because of the rather low magnitude of the aftershocks ($\leq M_L$ 5.4), they can only marginally contribute to the overall surface deformation pattern.

In this paper, we investigate the earthquake source and its main characteristics, benefiting from the large availability of DInSAR measurements. To do this we invert the available DInSAR deformation maps to retrieve the parameters characterizing the finite dislocation sources that we initially use to model the fault ruptures. Subsequently, we extend our modeling analysis through a 3D Finite Element (FE) numerical optimization, jointly exploiting the DInSAR measurements and a 3D model of the VF and GF, generated by integrating the available structural-geological and seismological information. This allows us to highlight the key role played by the configuration of the Gorzano-Vettore system, characterized by distinct faults at surface but interconnected at depth.

2. Exploited data

2.1 Structural data and fault model generation

The Quaternary extensional system of central Italy consists of well-exposed west-dipping, high-angle, normal faults, cross-cutting a pre-existing, Late Miocene in age, fold-and-thrust belt [Lavecchia et al., 1994]. Geological, geodetic, seismological data coherently highlight an active SW-NE tensional stress field [Ferrarini et al., 2015].

At the surface, the west-dipping faults consist of individual fault segments, extending 20-to-35 km along strike [Boncio et al., 2004], arranged in major alignments which may reach lengths of some hundreds of kilometers (**Figure 1a**). Since instrumental times, the alignment from Gubbio to L'Aquila has released three main normal-faulting earthquakes (Norcia 1979, M_w 5.9; Colfiorito 1997, M_w 6.0; L'Aquila 2009, M_w 6.3) [Lavecchia et al., 2011]; conversely, the most external alignment, after a long period of inactivity, was first marginally activated by some of the major aftershocks of the 2009 L'Aquila sequence (**Figure 1a**), and, seven years later, by the 2016 Central Italy seismic sequence. AEQ was located within the southern sector of the sequence; it nucleated at a depth of about 8 km, beneath the relay zone between the overlapping southern VF (Redentore-Vettoretto fault in **Figure 1b**) and northern GF segments (**Figure 1b**). The fault plane solution of AEQ and of the major events occurred in the following week, are almost purely extensional, with WSW-dipping preferential focal planes (**Figure 1c**). Their attitude closely recalls in strike, dip and rake the active outcropping faults (**Figures 1b, c).**

Relevant co-seismic fractures (CFs in **Figure 1c**) were generated for a continuous length of 5.8 km along the bedrock fault scarp of the southern end of the VF (the Redentore-Vettoretto fault) (**Figure 1e**). These CFs were characterized by average throw of 10-13 cm, with maximum values of 20-25 cm. More isolated CFs, with a down-throw of 1-2 cm, were also recognized along the GF (site **d** in **Figure S1**).

2.2 3D geometric fault model

The GF and VF 3D fault model has been generated by integrating, detailed fault traces (scale 1:25.000), fault-slip data, geological cross-sections, focal mechanisms and available hypocentral datasets (**Figures 1 and S1**).

In particular, to retrieve the GF surface, we integrated the structural-geological data with high-quality hypocentral locations of the northern half of L'Aquila 2009 aftershock sequence [Valoroso et al., 2013]. Depth contour lines of the southern GF already available in the literature were also considered [Lavecchia et al., 2012]. The GF surface extends for ~35 km along strike, dipping to WSW with an average of ~60° at depths <8 km and of ~50° at depths between 8-and-12 km (**Figures 1c, d**).

To retrieve the VF surface, we integrated the structural-geological information with the presently available seismological information [Gruppo di Lavoro INGV sul terremoto di Amatrice, 2016; TDMT in http://cnt.rm.ingv.it/tdmt.html].

The VF is articulated in two left-stepping sections (pink and grey areas in **Figure 1c**), with an overall length of 35 km and WSW dip-angles of 50° to 60°. At a depth of about 8 km, the GF and VF converge into a continuous surface, which extends in the N°155 direction, with an average dip of 50°, for a length of about 65 km. The stereo-projections of **Figure 1b** and **1c** highlight the very good fit in attitude among the outcropping faults, the surfaces reconstructed at depths and the preferential seismic planes from focal mechanisms.
Down-dip, the GF and VF surfaces were traced to reach a depth of 12 km coinciding with the calculated depth of base of the local seismogenic layer, intended as the depth above which the 90% of seismicity occurs (D90) (**Figure S2**).

2.3 DInSAR measurements

In our study, four interferograms have been exploited for the DInSAR analysis of the 2016 Amatrice earthquake. They are relevant to SAR image pairs acquired both from ascending and descending orbits and exhibiting good spatial coverage and interferometric coherence characteristics. In particular, two co-seismic ALOS2 and S1 interferograms, whose main information are reported in **Table S1**, were investigated. The analysis of these co-seismic DInSAR measurements revealed a spoon-like shape geometry of the detected surface deformation pattern (**Figures 2a, d**) characterized by two NNW-SSE striking main distinctive lobes. The ascending and descending DInSAR maps were also properly combined to retrieve the vertical and the East-West displacement components, which are reported in **Figures 2e, f.** Moreover, in order to mitigate the noise effects and achieve a significant improvement of the signal/noise ratio, we have applied a filtering step [Wiggin and Ender, 2001] to the retrieved surface deformation patterns. In particular, the contour maps of the filtered vertical co-seismic displacements are reported in **Figures 2g, 1.** We also observe that, despite the different shape of the lobes, they have nearly the same maximum deformation (about 20 cm) and overall extension (about 13 km^2). Finally, in terms of faulting mechanism, the hanging-wall block is affected by maximum subsidence that is located to the west of Gorzano-Vettore faults alignment (**Figure 2e**). This tendency is also supported by the E-W ground deformation component, which is consistent with a normal slip faulting mechanism (**Figure 2f**).

3. Source Investigation

3.1. Analytical modeling

In order to retrieve the seismogenic fault parameters responsible of the co-seismic displacements, we jointly inverted the selected ALOS2 and S1 DInSAR maps. Our modeling strategy follows a rather well established two-step approach [Solaro et al., 2016]: a non-linear inversion to estimate the fault planes parameters, followed by a linear inversion to retrieve the slip distribution on the fault planes. We first investigated a set of two finite dislocation planar sources in an elastic and homogeneous half-space [Okada, 1985], for which all sources parameters for both sources were set free during the inversion. The choice of using two planar sources in the optimization procedure is conditioned by the presence of two main distinctive lobes in the detected surface deformation patterns (**Figure 2**). In **Figure 3a** the best-fit parameters for the investigated two planar sources (referred to as Fault 1 and Fault 2) are summarized (see also **Figure S3**). Moreover, in order to have a more accurate estimate of the slip along the fault planes, a distributed slip was computed by partitioning the two planes into 20 x 10 patches. Also in this case we jointly inverted the selected ALOS2 and S1 DInSAR interferograms. To this aim, a linear inversion procedure has been performed by fixing the parameters of the non-linear inversion and searching for the differential slip on each patch, by inverting the following system of equations expressed in matrix form [Atzori et al., 2009]:

$$\begin{bmatrix} d_{DInSAR} \\ 0 \end{bmatrix} = \begin{bmatrix} G \\ k \cdot \nabla^2 \end{bmatrix} \bullet m$$

where $\mathbf{d_{DInSAR}}$ is the DInSAR data vector, **m** is the vector of unknown slip values, **G** is the Green's matrix with the point-source functions, $\boldsymbol{\nabla^2}$ is a smoothing Laplacian operator weighted by an empirical coefficient **k**. The system solution is obtained by means of the Singular Value Decomposition method. In this case, we found that the two causative faults are characterized by two main regions with a maximum slip of about 1.2 m at depth of 5-7 km along the two faults, located beneath the two main detected lobes (**Figures 3b, c**). The RMSE estimates of the residual displacements (i.e., the difference between measured and modeled displacements) were 3, 2.1, 2 and 2.9 cm for the ALOS2 descending, ALOS2 ascending, S1 descending and S1 ascending DInSAR maps, respectively.

Since the spatial orientation of the two planar solutions are very similar, we also investigated the possibility that a single but more extended planar fault might be capable of simulating the observed two lobes displacement pattern. The retrieved fault parameters are reported in **Figure 3d** (single fault) (see also **Figure S4**); in this case, the RMSE estimates were 3.1, 2.3, 2.1 and 3 cm for the ALOS2 descending, ALOS2 ascending, S1 descending and S1 ascending DInSAR maps, respectively, rather consistent with those obtained for the two-fault model. Moreover, the single fault modeling shows that the maximum slip is concentrated into two main patches at depths of 5-7 km (**Figures 3e, f**), very similar to the distributed slip pattern retrieved in the two-fault case. Therefore, our modeling results and DInSAR measurements suggest that it is not possible to uniquely discriminate which is the best configuration capable to simulate the surface displacement pattern between two coalescent faults or a single one. Accordingly, we have further extended our analysis by applying a numerical optimization procedure which allows us to take into account, in addition to the DInSAR measurements, the available structural-geological data.

3.2. Finite Element modeling

We implemented a 3D numerical model based on a FE method which jointly exploits the DInSAR measurements and the computed 3D fault mode. In particular, we analyzed the seismic event in a structural-mechanical context under the linear elastic mode to solve for the retrieved displacements. We considered an area extending for 80 × 80 km^2 (East and North directions, respectively) and with a depth of 15 km; such a large zone, with respect to the co-seismic epicentral region, allows us to assume the edge effects as negligible (**Figure 4a**). Within the developed heterogeneous model, we also assumed that the single geological units were isotropic and characterized by homogeneous mechanical properties. The entire numerical domain is discretized by considering 164.800 tetrahedral elements, with the elements size ranging from 250 m to 2.5 km. To reduce the computational effort, the mesh becomes coarser as the distance increases from the seismogenic fault. Boundary conditions were applied as follows: the upper boundary, representing the Earth's surface, was not constrained; the bottom boundary was fixed at a depth of 15 km, while rollers are applied at the four sides of the considered numerical domain. In addition, we assume specific internal boundary settings for the Gorzano-Vettore fault pattern in order to simulate the tectonic contacts among the achieved structural domains.

Concerning the model setup, it follows the approach presented in Tizzani et al., [2013]. In addition, we remark that the unlocked sectors of the Gorzano-Vettore fault pattern were modeled as contacts without frictional forces, the locked portions as identity pairs, while the bottom of the seismogenic layer surface as roller constraints. Our model evolves through two stages [Castaldo et al., 2016]: a gravitational stage is first applied, during which the initial state of stress is evaluated; subsequently, we model the co-seismic displacement field through the application of a couple of forces along the fault. This procedure is performed by assuming the geometry of the complex fault planes, constrained by the 3D structural information, and searching for the applied forces relevant to the hanging-wall and the foot-wall seismogenic patches. In particular, the best-fit solution is selected by searching for the minimum of the RMSE of the residuals (between the DInSAR and the modeled displacements). Specifically, as optimization tool we use the search grid method [Sen and Stoffa, 2013]. Details about the modelled fault parameters are provided in **Figure 4b**.

Our modeling approach allowed us to quantify the displacments relevant to the contacts of the hanging-all and footwall areas along both the VF and the GF, showing two well distinct zones of co-seismic displacements at a depth of about 5–7 km (**Figures 4c, d**). In particular, in the hanging-wall area the maximum displacement reaches a value of about 80 cm on the Norther Gorzano fault (NGF) and of 60 cm on the Redentore-Vettoretto fault (RVF) (**Figure 4c**). In the footwall area, we obtain a maximum total displacement of about 75 cm on the NGF and of 90 cm on the RVF (**Figure 4d**). Note also that the retrieved displacements in the footwall area of RVF significantly extend up to the surface, in rather good agreement with the in-situ surveyed ruptures which are particularly evident in this zone (see **Figure S1**).

Our solution, accounting also for the topography of the considered area, shows a very good fit with the observed ground deformations, both in terms of shape and amplitude of the residual signal. This is evident when comparing the best-fit solution for the ALOS2 (**Figures S5a, b**) and the S1 (**Figures S5c, d**) measurements, with the corresponding radar LOS-projected results of the FE model, respectively. In particular, the performed misfit analysis revealed rather small RMSE values for the achieved residuals, especially for the ALOS2 Ascending (RMSE = 1.1 cm) and S1 Ascending (RMSE = 1.3 cm); moreover, we found values of 2.4 cm and 3.1 cm for the ALOS2 and S1 Descending, respectively.

In order to further investigate the validity of our model, we have analyzed the co-seismic stress field distribution along the GF and VF segments, through the von Mises failure criteria [Negredo et al., 1999]. The von Mises stress field distribution (**Figure 4e**) showed that the highest stress magnitudes are located just in proximity of the intersection between the en-echelon GF and VF, which at a depth of about 8 km converge in a unified surface.

Finally, in the considered 2D cross-section we have reported the Vertical and EW components of the optimized displacement respectively (**Figures 4f, g**), and the associated von Mises stress field (**Figure 4h**). Note that the displacement vectors distribution further emphasize the asymmetrical motion of the hanging and footwall blocks. The maximum value of von Mises stress is reached at 8 km depth, in the hypocenter region.

4. Discussion and Conclusion

We have extensively exploited multi-sensor/multi-orbit DInSAR measurements relevant to the 24 August 2016 Amatrice earthquake (AEQ), to investigate the seismogenic source through analytical and numerical modeling techniques.

The starting point of our study has been the analysis of a set of ALOS2 and S1 co-seismic DInSAR maps which revealed a spoon-like shape geometry of the detected surface deformation pattern with two NNW-SSE striking main distinctive lobes, each of these characterized by nearly the same maximum vertical deformation (about 20 cm) and overall extension (about 13 km^2) (**Figure 2)**. These patterns could be considered as the effect induced by two distinct faults or due to the propagation of the rupture of a single fault. Accordingly, we have investigated both cases by considering a single and a double dislocation planar source in an elastic and homogeneous half-space. For both sources we retrieved two main regions with a maximum slip of about 1.2 m at depth of 5-7 km, beneath the two deformation lobes (**Figure 3**).

Nevertheless, the assessment of the spatial distribution of the residuals, based on RMSE analysis, did not allow us to uniquely discriminate which is the best-fit scenario between these two cases.

Accordingly, we have further extended our inversion of the DInSAR measurements by applying a numerical optimization procedure, in a 3D FE structural-mechanical environment. As *a priori* information, we introduce the independently generated geometric model of the Vettore and Gorzano faults (**Figure 1d**). This model shows a double fault system at depth shallower than 7-8 km and a single fault system at greater depths. The performed 3D FE modeling (**Figure 4**) is controlled by such an input geometry but it offers

a more realistic solution in light of the available geological and geophysical information. Furthermore, it allowed us to somehow conciliating the findings obtained from the single and double dislocation planar source inversion.

We found that, the retrieved best-fit co-seismic surface deformation pattern well supports the exploited structural model (**Figure S5**). Our 3D FE modeling results confirm that the maximum displacement occurred at a depth of about 5-7 km, affecting both the hanging wall and the footwall areas of the NGF and RVF. In particular, the displacement reached maximum values of 90 cm on the RVF footwall and of 80 cm on the NGF hanging wall.

Starting from the modelled displacement values and rupture area (about 180 km^2), we have computed a total seismic moment of about $2.5x10^{25}$ dyne·cm. This value indicates a moment magnitude of about M_w 6.2, which is slightly greater than that derived from TDMT [M_L 6.0, Tinti et al., 2016].

The retrieved von Mises stress field (**Figures 4e, h**) provides a good representation of the retrieved seismogenic scenario characterized by a bi-lateral rupture propagating on two distinct planes conjoined at the base; this rupture resulted in a stress change of 5-6 MPa, with respect to the lithostatic loading.

Our results may be relevant for a better comprehension of the use of active master fault segmentation pattern in defining the seismogenic potential of a zone and its seismic hazard. In fact, according to our hypothesis, the Amatrice earthquake did not nucleate within one of the intra-Apennine individual seismogenic sources [Boncio et al., 2004; Basili et al., 2008], but rather within the interlink zone at depth between two of them. This was just a preferential locus for concentrating shear traction and favoring earthquake nucleation.

To conclude, our analysis shows that the hypothesis of a bilateral rupture propagating along two en-echelon faults connected at the hypocentre is well supported. A bilateral rupture was previously highlighted by inversion of both strong motion [Calderoni et al., 2015] and GPS data [Gruppo di Lavoro INGV sul terremoto di Amatrice, 2016], but no conclusive information on the geometric configuration and earthquake-fault association are yet available. It is interesting to underline the peculiarity of the bilateral symmetric propagation characterising this normal fault earthquake. In such, AEQ is different from a larger percentage of Italian earthquakes [Tinti et al., 2014], which prevalently shows a unilateral propagation path.

This study provides insights on the seismogenic source of the 2016 Amatrice earthquake and, more generally, confirms the capability of our 3D FE approach to investigate complex earthquakes [Tizzani et al., 2013, Castaldo et al., 2016, Solaro et al., 2016], providing in this case a simple way to differentiate between approximately bilateral and predominantly unilateral ruptures. Future use of this approach can be relevant to both natural risks assessment and natural resources management/exploitation fields.

Acknowledgments

This work has been supported by the Italian Department of Civil Protection, the European Union Horizon 2020 research and innovation programme under grant agreement No 676564, the ESA GEP project and the I-AMICA project (Infrastructure of High Technology for Environmental and Climate Monitoring- PONa3_00363). Sentinel-1 data are copyright of Copernicus (2016). ALOS2 data are copyright of JAXA (2016) and they have been collected through the ALOS2 AO number P1101002. The DEMs of the investigated zone were acquired through the SRTM archive. We also thank Paul Lundgren and Simone Atzori for their helpful criticism and comments.

References

Atzori, S., I. Hunstad, M. Chini, S. Salvi, C. Tolomei, C. Bignami, S. Stramondo, E. Trasatti, A. Antonioli, and E. Boschi (2009), Finite fault inversion of DInSAR coseismic displacement of the 2009 L'Aquila earthquake (central Italy), *Geophys. Res. Lett*., 36, L15305, doi:10.1029/ 2009GL039293.

Barchi, M., (1991), Una Sezione geologica bilanciata attraverso il settore meridionale dell'Appennino Umbro-Marchigiano: L'Acquasparta-Spoleto-Accumoli. In: Pialli G., Barchi M.R., and Menichetti M. (eds) Studi preliminari all' acquisizione dati del profilo CROP 03 Punta Ala-Gabicce. *Studi Geologici Camerti*, 1, 347–362.

Basili R., G. Valensise, P. Vannoli, P. Burrato, U. Fracassi, S. Mariano S., M.M. Tiberti and E. Boschi (2008), The Database of Individual Seismogenic Sources (DISS), version 3: Summarizing 20 years of research on Italy's earthquake geology, *Tectonophysics*, 453, 20–43.

Boncio, P., G. Lavecchia, and B. Pace (2004), Defining a model of 3D seismogenic sources for Seismic Hazard Assessment Applications: the case of central Apennines (Italy), *J. Seismol.*, 8(3), 407-425.

Brozzetti, F., and G. Lavecchia (1994), Seismicity and related extensional stress field: the case of the Norcia seismic zone (central Italy), *Annales Tectonicae*, 8, 36-57.

Calderoni, G., A. Rovelli, Y. Ben-Zion, and R. Di Giovambattista (2015), Along-strike rupture directivity of earthquakes of the 2009 L'Aquila, central Italy, seismic sequence, *Geophys. J. Int.*, 203(1), 399-415.

Castaldo, R., V. De Novellis, G. Solaro, S. Pepe, P. Tizzani, C. De Luca, M. Bonano, M. Manunta, F. Casu, I. Zinno, and R. Lanari (2016), Finite element modelling of the 2015 Gorkha earthquake through the joint exploitation of DInSAR measurements and geologic-structural information, *Tectonophysics*, doi: 10.1016/j.tecto.2016.06.037.

Chiarabba, C., P. De Gori, and F. M. Mele (2015), Recent seismicity of Italy: Active tectonics of the central Mediterranean region and seismicity rate changes after the Mw 6.3 L'Aquila earthquake, *Tectonophysics*, doi:/10.1016/j.tecto.2014.10.016

Ferrarini, F., G. Lavecchia, P. Boncio, R. de Nardis, G. Pappone, M. Cesarano, and P.P.C. Aucelli (2015), Clues of structural inheritance and localized reactivation along a Quaternary active normal fault system (Molise, Central Italy), *Rend. Online Soc. Geol. It.*, Suppl. n. 1 al Vol. 36.

Franceschetti, G. and R. Lanari (Eds) (1999) *Synthetic Aperture Radar Processing*, CRC Press, New York.

Gruppo di Lavoro INGV sul terremoto di Amatrice (2016), Secondo rapporto di sintesi sul Terremoto di Amatrice M_L 6.0 del 24 Agosto 2016 (Italia Centrale), doi: 10.5281/zenodo.154400.

Lavecchia, G. (1985), I1 sovrascorrimento dei Monti Sibillini: analisi cinematica e strutturale. *Bollettino della Societa Geologica Italiana* 104, 161-194.

Lavecchia, G., F. Brozzetti, M. Barchi, M. Menichetti, and J.V.A. Keller (1994), Seismotectonic zoning in east-central Italy deduced from an analysis of the Neogene to present deformations and related stress fields, *Geol. Soc. Am. Bull.*, 106, 1107–1120.

Lavecchia, G., P. Boncio, F. Brozzetti, R. de Nardis, D. Di Naccio, F. Ferrarini, A. Pizzi and G. Pomposo (2011), The April 2009 L'Aquila (Central Italy) seismic sequence (Mw 6.3): A preliminary seismotectonic picture. In: Recent Progress on Earthquake Geology (Guarnieri P., ed.), Nova Science Publishers, New York, 1-17.

Lavecchia, G., F. Ferrarini, F. Brozzetti, R. de Nardis, P. Boncio, and L. Chiaraluce (2012), From surface geology to aftershock analysis: Constraints on the geometry of the L'Aquila 2009 seismogenic fault system,*Ital. J. Geosci*., *131*(3), 330-347.

Negredo, A.M., E. Carminati, S. Barba, and R. Sabadini (1999), Dynamic modelling of stress accumulation in central Italy. *Geophys. Res. Lett*., 26. N.13 1945-1948.

Okada, Y. (1985), Surface deformation due to shear and tensile faults in a half-space, *Bull. Seismol. Soc. Am.*, 75, 1135– 1154.

Sen M. K. and P.L. Stoffa (2013), Global optimization methods in geophysical inversion. *Cambridge University Press*.

Sibson, R.H. (1984), Roughness at the base of the seismogenic zone: contributing factors, *J. Geophys. Res.*, 89, 5791–5799.

Solaro, G., V. De Novellis, R. Castaldo, C. De Luca, R. Lanari, M. Manunta, and F. Casu (2016), Coseismic Fault Model of Mw 8.3 2015 Illapel Earthquake (Chile) Retrieved from Multi-Orbit Sentinel1-A DInSAR Measurements, *Remote Sensing*, 8, 323; doi:10.3390/rs8040323.

Tinti, E., L. Scognamiglio, A. Cirella, and M. Cocco (2014), Up-dip directivity in near-source during the 2009 L'Aquila main shock, *Geophys. J. Int.*, 198, 1618-1631.

Tinti, E., L. Scognamiglio, A. Michelini, and M. Cocco (2016), Slip heterogeneity and directivity of the ML 6.0, 2016, Amatrice earthquake estimated with rapid finite-fault inversion, *Geophys. Res. Lett.*, 43, doi:10.1002/2016GL071263.

Tizzani, P., R. Castaldo, G. Solaro, S. Pepe, M. Bonano, F. Casu, M. Manunta, M. Manzo, A. Pepe A., S. Samsonov, R. Lanari, and E. Sansosti (2013), New insights into the 2012 Emilia (Italy) seismic sequence through advanced numerical modeling of ground deformation InSAR measurements, Geophys. Res. Lett., 40, 1–7, doi:10.1002/2012GL054921.

Valoroso, L., L. Chiaraluce, D. Piccinini, R. Di Stefano, D. Schaff and F. Waldhauser (2013), Radiography of a normal fault system by 64,000 high-precision earthquake locations: The 2009 L'Aquila (central Italy) case study, J. Geophys. Res., 118, 1156-1176, doi:10.1002/jgrb.50130.

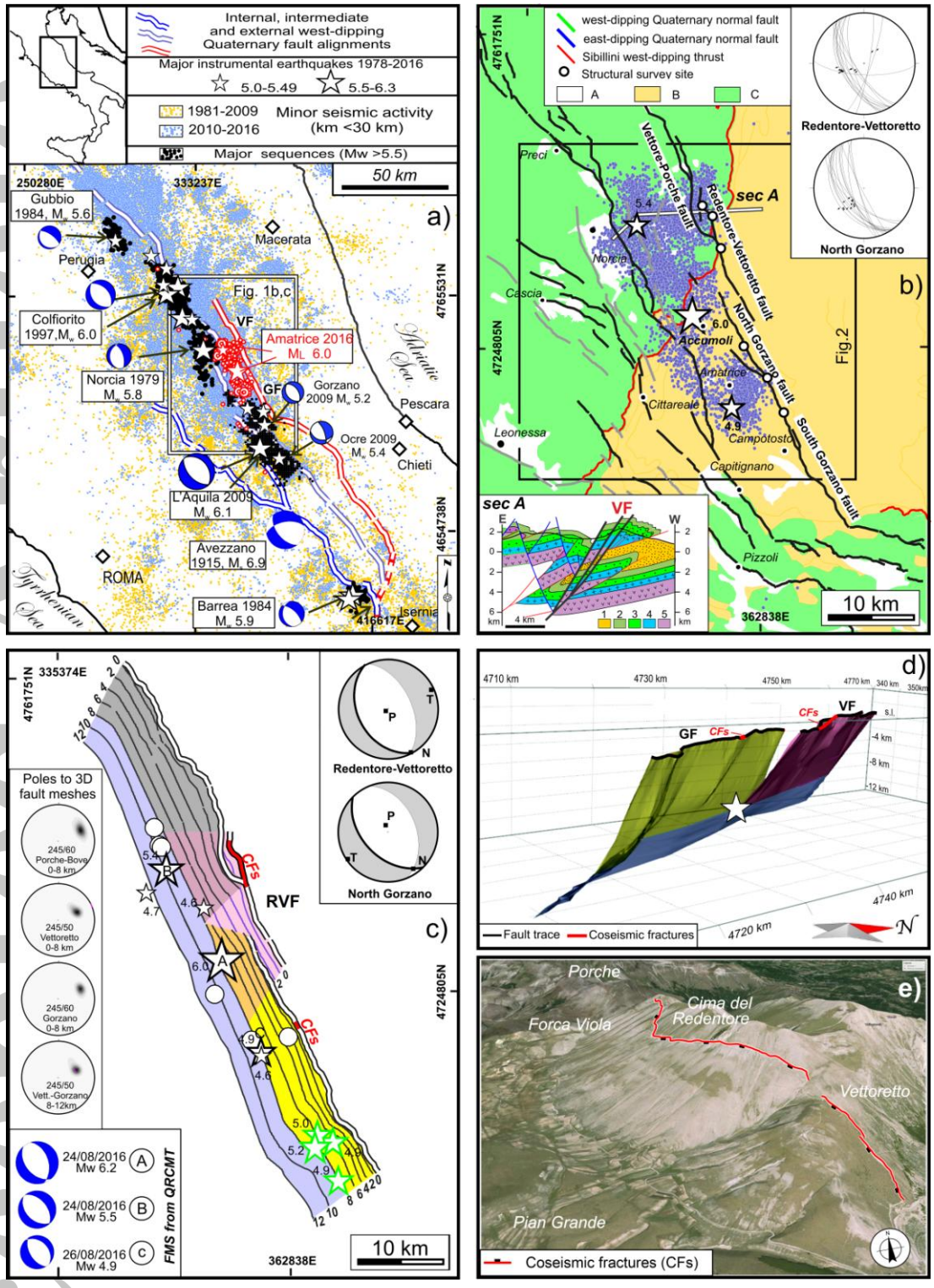

Figure 1. Seismotectonic framework. (**a**) Background seismicity since 1981, with major instrumental sequences and active fault alignments [Lavecchia et al., 2012]. (**b**) Amatrice earthquake epicentral area (24-to-31 August 2016), with active normal faults and pre-existing compressional structures (A: Quaternary continental deposits, B: Meso-Cenozoic marly-carbonate multilayer; C: late Miocene siliciclastic sediments); the stereonets report newly fault-slip data; the geologic section is from Brozzetti and Lavecchia [1994] (1: siliciclastic

deposits, 2,3,4 carbonate multilayer, 5: Triassic evaporites). (**c**) Depth contour lines of the Vettore-Gorzano fault alignment, with main hypocenters of the Amatrice 2016 sequence (white dots and stars) and of the northernmost L'Aquila 2009 sequence (green stars); the stereonets on the upper right corner report average Amatrice fault plane solutions for events with M_W>3.5, TDMT focal mechanisms available at http://cnt.rm.ingv.it/tdmt.html; the stereonets on the left represent density contour of poles to Gorzano and Vettore surfaces as built in panel (d). (**d**) Computed 3D fault model; the traces of the cross-sections used for the reconstruction are given in **Figure S1a**. (**e**) Google map image of the Mt. Vettore with, highlighted in red, the trace of the coseismic fractures (CFs) surveyed along the RVF; CFs location is in panel (c).

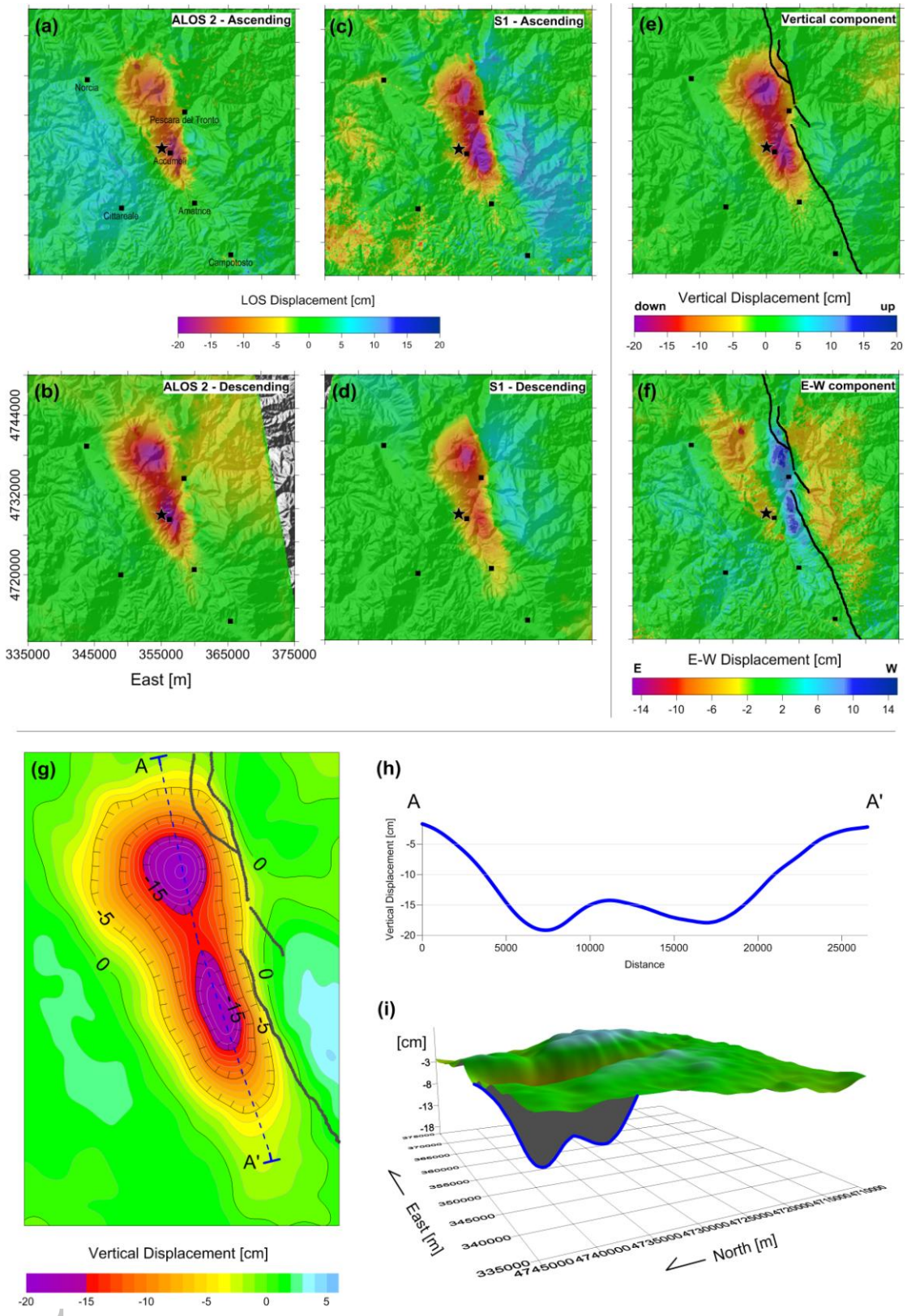

Figure 2. DInSAR measurements. (**a, b**) DInSAR (LOS) maps computed by using ALOS2 data acquired (**a**) from ascending orbits on September 09, 2015 and August 24, 2016, and (**b**) from descending orbits on May 25, 2016 and August 31, 2016. (**c, d**) DInSAR (LOS) maps computed by using S1 data acquired (c) from ascending orbits on August 15-27, 2016, and

(**d**) from descending orbits on August 21-27, 2016. (**e, f**) Surface deformation components computed from both ascending (**a, c**) and descending (**b, d**) DInSAR maps: (**e**) vertical deformation component; (**f**) east–west deformation component. The black star indicates the main shock location. (**g**) Contour map obtained following a spatial filtering step. (**h**) Plot along the AA' section encompassing the region of maximum ground deformation lobes. (**i**) A 3D view of the vertical deformation pattern.

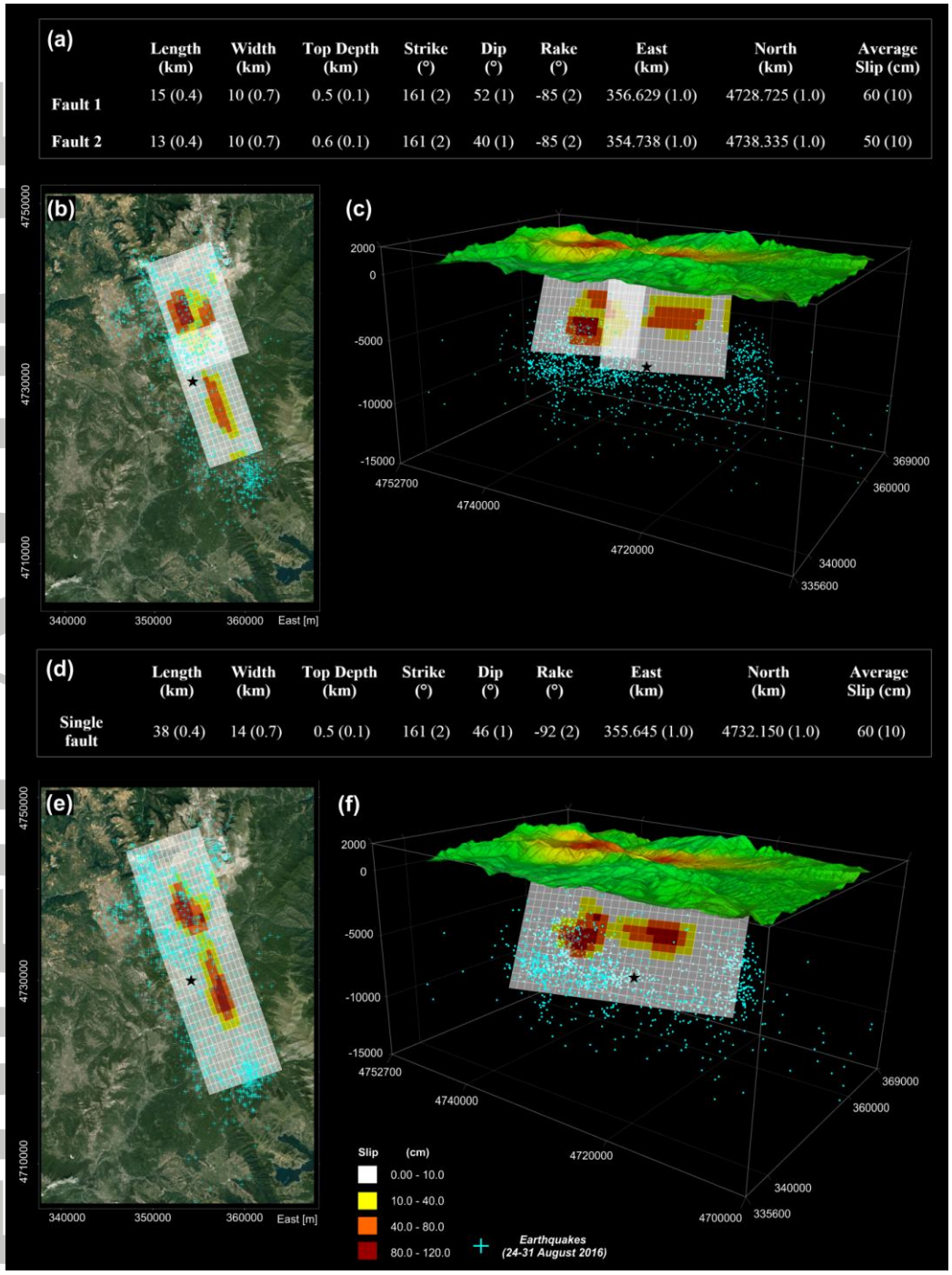

Figure 3. Coseismic slip distribution retrieved through the Okada inversion. (**a**) Fault parameters retrieved from the two fault inversion; (**b, c**) distributed slip (over 20 x 10 patches, each of these extending for about 0.8 x 1.0 km^2) displayed in (**b**) map view and (**c**) 3D view. (**d**) Fault parameters retrieved from the single fault inversion, (**e, f**) distributed slip (over 28 x 16 patches, each of these extending for about 1.6 x 0.8 km^2) displayed in (**e**) map view and (**f**) 3D view. The aftershock distribution, with $M_L > 2$, spanning from August 24 to 31 (corresponding to the last day of the satellite SAR data temporal coverage) are depicted with cyan crosses; the black star indicates the main shock location.

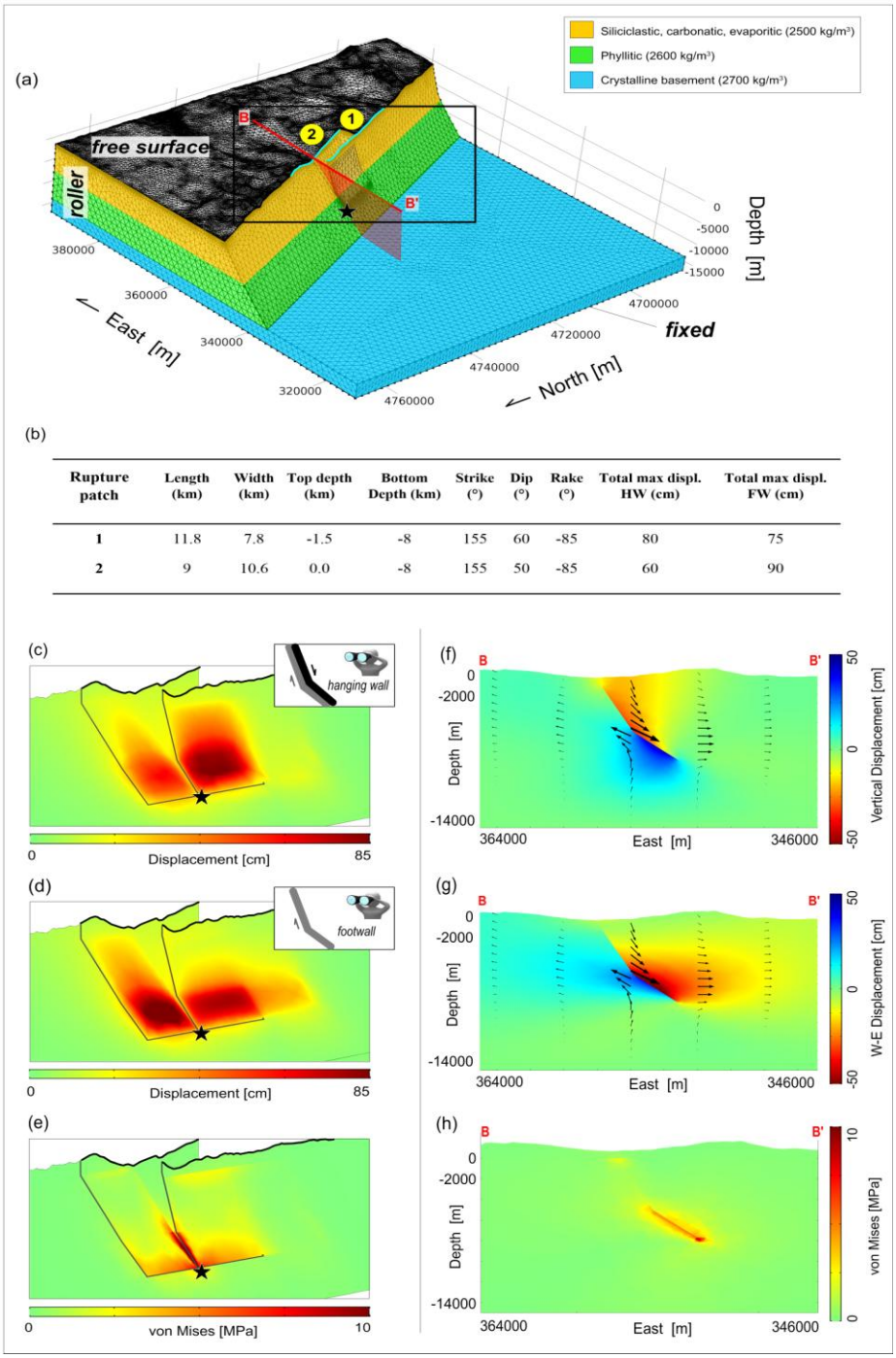

Rupture patch	Length (km)	Width (km)	Top depth (km)	Bottom Depth (km)	Strike (°)	Dip (°)	Rake (°)	Total max displ. HW (cm)	Total max displ. FW (cm)
1	11.8	7.8	-1.5	-8	155	60	-85	80	75
2	9	10.6	0.0	-8	155	50	-85	60	90

Figure 4. 3D FE modeling results. (**a**) Setup of the performed FE model showing the numerical domain discretization with the locations of the NGF (labelled as 1) and RVF (labelled as 2). The boundary conditions and subdomains setting are also reported. (**b**) Estimated fault parameters. (**c**) Amplitude of the retrieved displacements (relevant to the black rectangle area in panel (a)) showed in 3D view to emphasize the dislocation effect on the hanging-wall of RVF and NGF. (**d**) Same of (c), but relevant to the footwall side. (**e**) von Mises stress distribution showed in 3D view. All views represent the co-seismic effects recorded on the hanging-wall side. (**f, g, h**) Results relevant to the selected 2D cross-section

(N=4733000) identified in panel (a) by the red segment BB'. In particular, we show the Vertical (**f**) and EW (**g**) components of the retrieved displacements and the von Mises stress fields (**h**), respectively; the black arrows indicate the direction along the profile of the 3D displacement field. The black star indicates the main shock location.